Nano Energy 70 (2020) 104548

Contents lists available at ScienceDirect

Nano Energy

journal homepage: http://www.elsevier.com/locate/nanoen

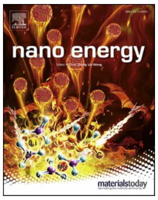

Communication

Dual carbon decorated $Na_3MnTi(PO_4)_3$: A high-energy-density cathode material for sodium-ion batteries

Ting Zhu [a,1], Ping Hu [a,1], Congcong Cai [a], Ziang Liu [a], Guangwu Hu [a], Quan Kuang [b], Liqiang Mai [a], Liang Zhou [a,*]

[a] State Key Laboratory of Advanced Technology for Materials Synthesis and Processing, Wuhan University of Technology, Wuhan, 430070, China
[b] School of Physics and Optoelectronics, South China University of Technology, Guangzhou, 510641, China

ARTICLE INFO

Keywords:
NASICON structure
$Na_3MnTi(PO_4)_3$
Double carbon decoration
Cathode material
Sodium-ion battery

ABSTRACT

NASICON-structured $Na_3MnTi(PO_4)_3$ (NMTP) is a high-energy sodium-ion battery (SIB) cathode material. However, the low rate capability and unsatisfactory cycle life limit its practical applications. Herein, a dual carbon decoration strategy has been proposed to tackle the above-mentioned issues of NMTP. The semi-graphitic carbon and reduced graphene oxide co-functionalized NMTP (NMTP/C@rGO) demonstrates a specific capacity of ~114 mAh g^{-1}, reaching a high energy density of ~410 Wh kg^{-1} with an average discharge potential of ~3.6 V. Besides, the NMTP/C@rGO also manifests long-term durability and high rate capability. More importantly, the NMTP/C@rGO also demonstrates ideal electrochemical properties in NMTP/C@rGO//soft carbon full cells. The impressive electrochemical performances make the NMTP/C@rGO a reliable cathode material for SIBs.

1. Introduction

Sodium-ion batteries (SIBs) have become a promising candidate, which aroused explosive enthusiasm of the researchers recently, to compensate lithium-ion batteries (LIBs) in energy storage [1–9]. This can be ascribed to the analogous operating principles of SIBs and LIBs as well as the cheapness and profusion of Na resources. To push the practical application of SIBs in large scale energy storage, efforts have been dedicated to improving the energy/power density, cycle life, and safety [10–13].

The cathode represents one of the most important components for SIBs. Tremendous efforts have been dedicated to seeking suitable cathode materials, such as Prussian blue analogues [14–16], layered oxides [17–22], and polyanionic compounds [23–27]. Although the Prussian blue analogues possess an open framework structure with large interstitial sites, they suffer from poor thermal stability, low volumetric density, and toxicity. The layered oxides have high theoretical capacity, while the structural instability and unsatisfactory cycle life extensively limit their applications. Polyanionic compounds have aroused great attention due to their robust crystal structure with excellent thermal stability, small volume change during sodium ion intercalation/de-intercalation, and high safety.

Among the polyanionic compounds, Na superionic conductor (NASICON)-structured materials possess a unique framework, endowing the material three-dimensional channels for fast Na^+ mobility [28–30]. As one of the most famous NASICON-structured material, $Na_3V_2(PO_4)_3$ (NVP) has a theoretical capacity of 117 mAh g^{-1} with a flat plateau at 3.3–3.4 V [31]. Considering the toxicity and relatively high cost of V, increasing attention has been paid to partial/entire substitution of V with other elements, such as Mn, Fe, Ni, Ti, Cr, Mg, etc. [1,32–39] Lavela and co-workers replaced 10% of the V with Cr and obtained $Na_3V_{1.8}Cr_{0.2}(PO_4)_3$ with a high plateau at ~3.8 V [33]. The Cr doping amount could be further increased to 50% in this case. Goodenough et al. reported a series of NASICON-structured $Na_xMV(PO_4)_3$ compounds with half of the V in NVP being substituted, in which M represents Mn, Fe, and Ni [35]. Among these materials, the $Na_4MnV(PO_4)_3$ exhibited two high plateaus at ~3.6 and 3.4 V *vs.* Na^+/Na, corresponding to the $Mn^{2+/3+}$ and $V^{3+/4+}$ redox couples, respectively. Such high plateaus could lead to a high energy density as demonstrated by Zhang and Jiao et al. in their recent study [36]. Recently, NASICON-structured $Na_3MnTi(PO_4)_3$ (NMTP) was reported by Goodenough and co-workers [40]. This material possesses three redox couples: $Mn^{3+/4+}$ (~4.1 V), $Mn^{2+/3+}$ (~3.6 V), and $Ti^{3+/4+}$ (~2.1 V *vs.* Na^+/Na). When the three-electron redox reaction is realized, its theoretical capacity can reach 176 mAh

---

[*] Corresponding author.
E-mail address: liangzhou@whut.edu.cn (L. Zhou).
[1] These authors contributed equally to this work.

https://doi.org/10.1016/j.nanoen.2020.104548
Received 4 December 2019; Received in revised form 28 January 2020; Accepted 28 January 2020

g^{-1} [41]. Aside from the high theoretical capacity and high plateaus, the replacement of V with Mn and Ti can bring advantages such as lower toxicity and lower cost. Thus, the NMTP has been recognized as an immensely promising high-energy cathode material for SIBs. Despite the above-mentioned favorable characteristics, the NMTP suffers from disappointing electronic conductivity, which may lead to unsatisfactory cycling stability and rate performance.

Herein, we propose a dual carbon decoration strategy to boost the rate capability and cyclability of NMTP. Semi-graphitic carbon and reduced graphene oxide co-functionalized NMTP microspheres (NMTP/C@rGO) have been constructed by a spray-drying approach. The obtained NMTP/C@rGO manifests a considerable capacity of ~114 mAh g^{-1} with an average potential of ~3.6 V *vs.* Na^+/Na, affording a high energy density of ~410 Wh kg^{-1}. Apart from high energy density, the NMTP/C@rGO also demonstrates long-term durability and high rate capability. After 800 cycles at 1 C (1 C = 117 mA g^{-1}), 76% of the capacity can be retained. When coupled with soft carbon, the NMTP/C@rGO also demonstrates good cycling stability in NMTP/C@rGO//soft carbon full cells.

2. Experimental section

2.1. Preparation of NMTP/C@rGO

The NMTP/C@rGO was prepared by a spray-drying approach with post-annealing. 15 mmol $NaH_2PO_4 \cdot 2H_2O$, 5 mmol $Mn(CH_3COO)_2 \cdot 4H_2O$, 5 mmol $C_6H_{18}N_2O_8Ti$, and 10 mmol $C_6H_8O_7 \cdot H_2O$ were dissolved in water. After adding 50 mL of graphene oxide solution (GO, 2 mg mL^{-1}) to the above solution, the suspension was spray dried. The intermediate collected after spray drying was annealed in Ar for 4 h at 600 °C to obtain the NMTP/C@rGO. The control sample, NMTP/C, was synthesized with a similar method without the introduction of GO. The NMTP/C@rGO-550 and NMTP/C@rGO-650 were synthesized by varying the annealing temperature to 550 and 650 °C, respectively.

2.2. Material characterization

Phase analyses were implemented by a Bruker D8 Advance X-ray diffractometer in a 2θ range of 10–80°, which equipped with a non-monochromated Cu Kα X-ray with λ = 1.5418 Å. The microstructure was analyzed by field-emission scanning electron microscopy (SEM, JEOL-7100F), transmission electron microscopy (TEM), and high-angle annular dark-field scanning TEM (HAADF-STEM, JEOL JEM-2100F) equipped with energy-dispersive spectroscopy (EDS, Oxford EDS IE250). Thermogravimetric analysis (TGA) was performed in air with a temperature ramping rate of 10 °C min^{-1} using an STA-449C thermobalance. X-ray photoelectron spectroscopy (XPS) characterizations were performed on a VG Multilab 2000 instrument. Raman spectra were recorded by a Horiba LabRAM HR Evolution (532 nm laser). The N_2 sorption results were measured by a Tristar II 3020 instrument.

In-situ XRD experiment was performed on a Bruker D8 Advance X-ray diffractometer. The electrode was placed behind an X-ray transparent Be window. The signals were collected in a still mode with a planar detector during the charge/discharge process and each pattern was acquired in 120 s. The cathode was composed of active material, acetylene black, and polytetrafluoroethylene with a mass ratio of 6: 3: 1. The loading mass of the active material was roughly 1.2–1.8 mg cm^{-2}.

2.3. Measurement of electrochemical characterization

Electrochemical tests were measured by assembling 2016 coin-type cells. The cathode was composed of active material, acetylene black, and polyvinylidene fluoride (PVDF) with a mass ratio of 7: 2: 1. Sodium disks were employed as the anode, 1.0 M $NaClO_4$ in EC/PC (1:1 w/w) with FEC (5 wt%) was used as the electrolyte, and the separator was grade GF/D. Cyclic voltammetry (CV) test and electrochemical impedance spectroscopy (EIS) were implemented using electrochemical CHI600E and Autolab PGSTAT 302 N workstations, respectively. Galvanostatic charge/discharge tests were performed on the LAND CT2001A in the potential range of 2.5–4.2 V *vs.* Na^+/Na.

3. Results and discussion

The NMTP/C@rGO was synthesized through a spray drying method with subsequent high-temperature annealing. This method has two obvious merits. (I) Spray drying has been extensively employed in food and pharmaceutical industries and it is feasible for mass production. (II) The product has a microspherical morphology with minimized aggregation, which is beneficial for achieving high packing density.

The XRD pattern and Rietveld refinement are presented in Fig. 1a. The XRD pattern can be indexed to pure phase NASICON-structured NMTP with rhombohedral R-3c space group, agreeing well with previous literature [40-42]. More detailed structural information, such as lattice parameters, atomic coordinates, and occupancy, is listed in Table S1. The occupancy factors for Na (1) and Na (2) are 0.981 and 0.673, respectively. According to the occupancy, the total Na in a unit cell (Z = 6) is calculated to be 18, in well consistent with the chemical formula. The schematic structure of NMTP/C@rGO is also provided based on the Rietveld refinement results (Fig. 1b). The XRD pattern of NMTP/C resembles that of NMTP/C@rGO (Fig. S1). For both samples, no impurity diffraction can be detected, confirming their high purity.

The TGA curve of NMTP/C@GO (Fig. 1c) shows a total mass loss of 7.95 wt%. It should be noted that a slight weight gain is observed at 480–520 °C, which is mainly caused by the oxidation of Mn(II). From the TGA curves, the carbon content of NMTP/C@rGO is slightly higher than that of NMTP/C (6.86 wt%). For both NMTP/C@rGO and NMTP/C, the intensity of D-band (1350 cm^{-1}) is slightly lower than that of G-band (1580 cm^{-1}) in Raman spectra (Fig. 1d), suggesting the partially graphitized characteristic of carbon in both samples. N_2 sorption experiments were used to determine the surface area and pore volume of NMTP/C@rGO and NMTP/C (Fig. S2). The NMTP/C@rGO manifests a higher surface (33.56 *vs.* 2.23 m^2 g^{-1}) but lower pore volume (0.31 vs. 0.52 cm^3 g^{-1}) than the NMTP/C.

The NMTP/C@rGO shows well-defined microsphere morphology with a relatively rough surface (Fig. 2a). The size of microspheres ranges from 0.3 to 5 μm. TEM images (Fig. 2b–c) reveal that the NMTP/C@rGO solid microspheres are assembled by a large number of irregular nanoparticles. High-resolution TEM image (Fig. 2d) of NMTP/C@rGO displays lattice fringes of 0.21 and 0.44 nm, corresponding to the (303) and (104) crystal planes of NASICON structured NMTP, respectively. Besides, a semi-graphitic carbon layer can be observed on the surface. The HAADF-STEM image and the corresponding EDS mappings show that each element is distributed uniformly throughout the entire NMTP/C@rGO microsphere. Acid etching treatment was carried out for NMTP/C@rGO to study the microstructure of carbon matrix. The acid etching removes most of the NMTP and leaves behind a continuous carbon matrix (Fig. S3). Such a continuous carbon matrix wires the NMTP in the composite. The control sample, NMTP/C, exhibits a similar microspherical morphology to NMTP/C@rGO (Fig. S4). The major difference is that the NMTP/C possesses a hollow microsphere structure, which may be caused by the foaming of citric acid during spray drying/pyrolysis. With the introduction of GO, the foaming of citric acid is restricted and solid microspheres can be obtained. Given the solid spherical structure of NMTP/C@rGO and the hollow spherical structure of NMTP/C, the former demonstrates an obviously higher packing density than the later (Fig. S5).

The Na storage properties of NMTP/C@rGO were measured in CR2016 type coin cells using sodium disks as the anodes. The CV profiles (Fig. 3a) display two pairs of oxidation/reduction peaks located at 3.73/3.43 and 4.14/3.94 V, which can be assigned to the $Mn^{2+/3+}$ and $Mn^{3+/4+}$ redox couples, respectively. It should be mentioned that a weak anodic peak can also be observed at around 3.98 V. However, this peak

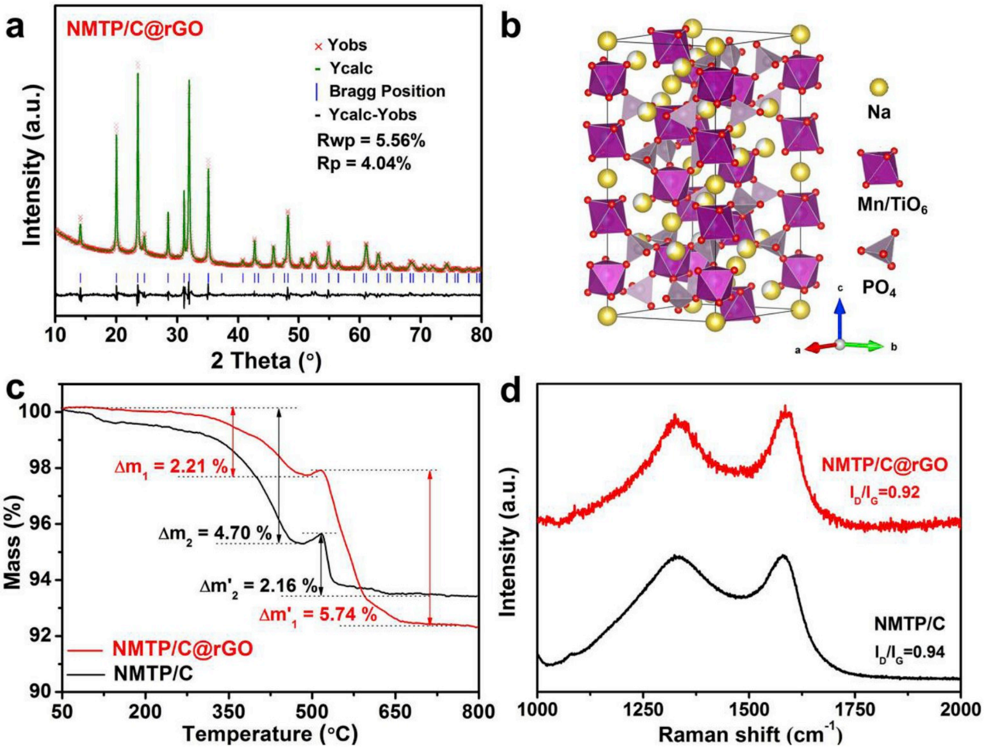

Fig. 1. (a) Rietveld refinement of the XRD pattern and (b) the schematic structure of the NMTP/C@rGO. The MnO_6 and TiO_6 octahedra are presented in magenta, the PO_4 octahedra are in light purple, and the sodium ions are in golden. (c) TGA curves and (d) Raman spectra of the NMTP/C@rGO and NMTP/C.

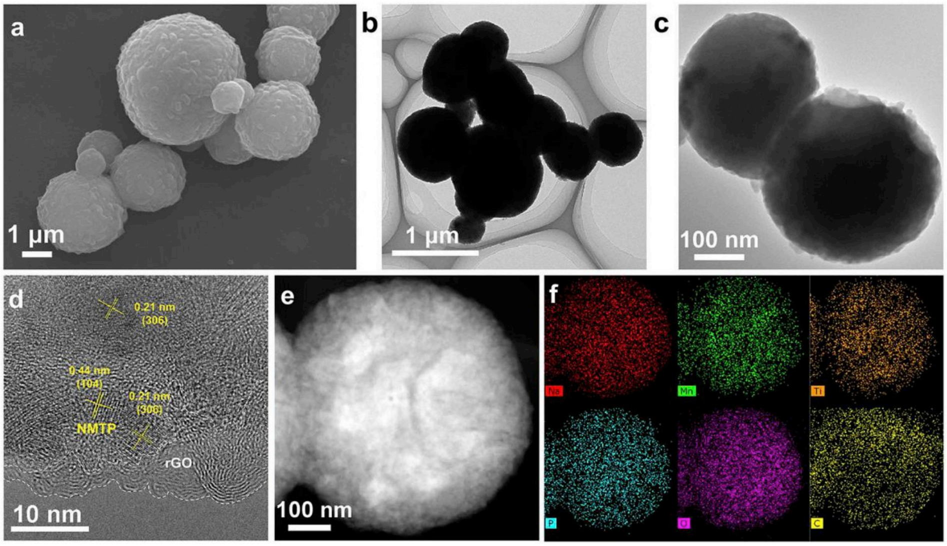

Fig. 2. (a) SEM, (b, c) TEM, and (d) HRTEM images of NMTP/C@rGO; (e) HAADF-STEM image of NMTP/C@rGO and (e) the corresponding elemental mapping of sodium (red), manganese (green), titanium (orange), phosphorus (blue), oxygen (purple), and carbon (yellow).

cannot be assigned to any known oxidation process currently. The CV profiles overlap quite well, demonstrating the excellent reversibility of Na^+ de-intercalation/intercalation processes in NMTP/C@rGO. The two pairs of redox peaks can also be explicitly observed even at high scan rates, indicating the good rate capability of NMTP/C@rGO microspheres (Fig. S6).

Fig. 3b and c show the charge/discharge curves of NMTP/C@rGO and NMTP/C at various rates, respectively. Obvious charge/discharge plateaus can be observed, agreeing well with the presented CV curves. The NMTP/C@rGO displays discharge capacities of 114, 112, 97, 78, and 61 mAh g^{-1} at 0.2, 0.5, 1, 2, and 5 C, respectively (Fig. 3d). Considering the average discharge potential of ~3.6 V and a discharge capacity of 114 mAh g^{-1}, the energy density of NMTP/C@rGO reaches up to 410 Wh kg^{-1}. When the C-rate returns to 0.2 C after cycled 50 times, 94% of the initial discharge capacity can be recovered (107 mAh g^{-1}). In contrast, for NMTP/C microspheres, a relatively low discharge capacity of 62 mAh g^{-1} is obtained after 50 cycles. The NMTP/C@rGO exhibits higher medium discharge voltage platforms (~3.5 V *vs.* Na^+/Na) than the NMTP/C, especially at high current densities (Fig. S7) [43]. Interestingly, the medium discharge voltage of NMTP/C@rGO at 5 C is higher than those at lower C-rates. This is because the NMTP/C@rGO displays a low voltage plateaus at around 2.55 V, and this low voltage

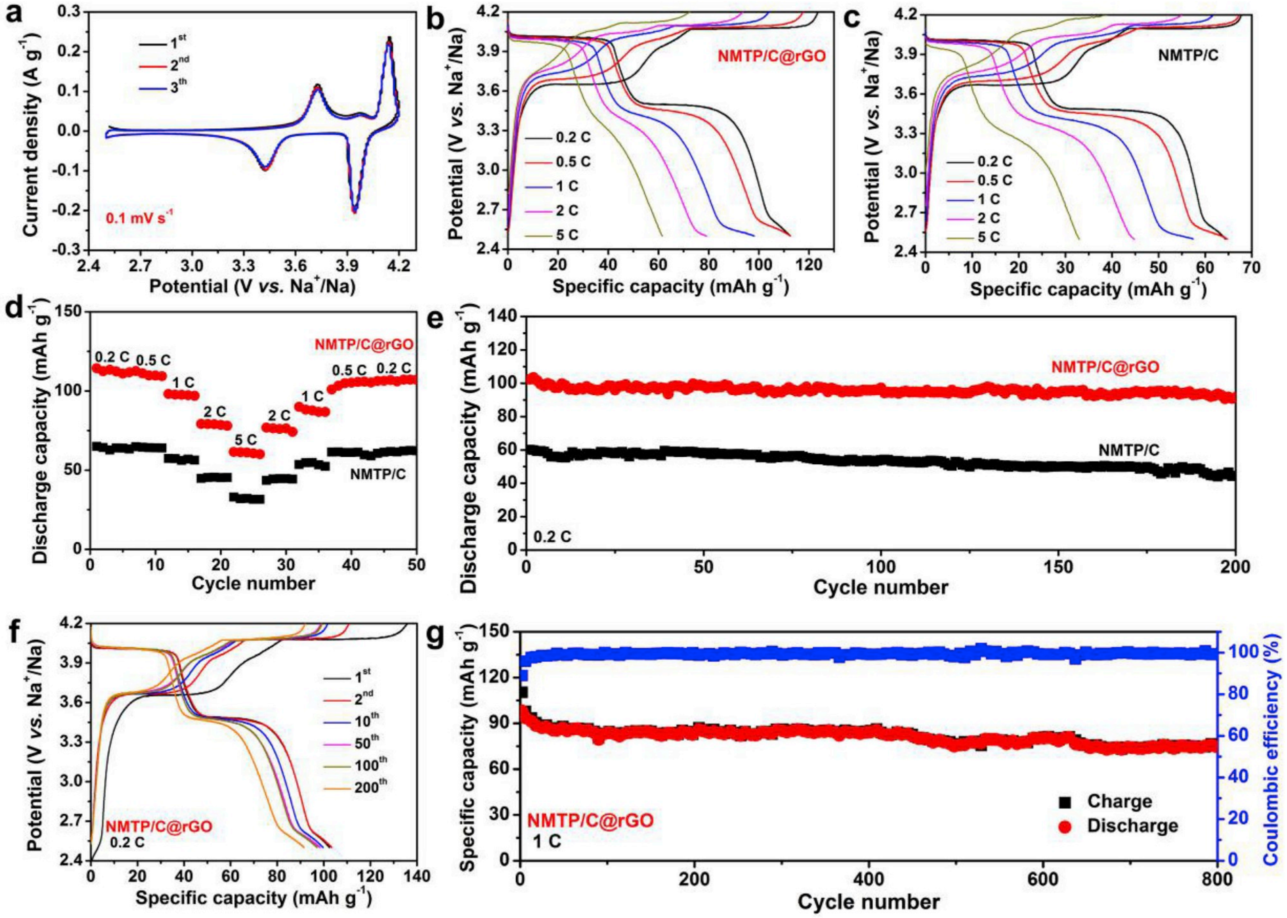

Fig. 3. Electrochemical performances of NMTP/C@rGO and NMTP/C in the electrochemical window of 2.5–4.2 V *vs.* Na^+/Na. (a) Cyclic voltammogram of NMTP/C@rGO at a scan rate of 0.1 mV s^{-1}. Charge/discharge curves of (b) NMTP/C@rGO and (c) NMTP/C at different rates. (d) Rate performances of the two materials. (e) Cycling performances of the two materials at 0.2 C. (f) Representative charge/discharge curves of NMTP/C@rGO at 2 C. (g) Long-term cycling performance of NMTP/C@rGO at 1 C.

plateau disappears at 5 C due to the polarization at a high rate.

Besides higher specific capacity and discharge plateaus, the NMTP/C@rGO also demonstrates better cyclability than the NMTP/C. At 0.2 C, the capacity retention of NMTP/C@rGO is 89.4% after 200 cycles, much higher than that of NMTP/C (73.9%) (Fig. 3e and f, and S8). At a relatively high rate of 1 C, the NMTP/C@rGO delivers a capacity of 98 mAh g^{-1} and retains 76.6% of the capacity after 800 cycles (Fig. 3g), further testifying the excellent cyclability. When compared to recently reported NASICON structured bi-metal phosphate SIB cathode materials, the NMTP/C@rGO manifests very high energy density with a moderate power density (Fig. S9) [34,42–47]. Meanwhile, the Mn and Ti resources are relatively cheap and pollution-free.

The Na storage performance NMTP/C@rGO at a high temperature of 50 °C is also investigated. At 50 °C, the NMTP/C@rGO delivers a capacity of 92 mAh g^{-1} at 1 C and maintains ~82% of the capacity after 200 cycles (Fig. S10). This result indicates the NMTP/C@rGO exhibits an excellent Na storage performance at a relatively high temperature. The Na storage performance of NMTP/C@rGO in the potential window of 1.5–4.2 V has also been investigated (Fig. S11). An additional discharge plateau appears at ~2.1 V ($Ti^{3+/4+}$) in this potential window, giving rise to a high discharge capacity of 149 mAh g^{-1} at 0.7 C (1 C = 176 mAh g^{-1}). Besides, the high capacity doesn't compromise the cycling stability; a capacity of 132 mAh g^{-1} can be achieved after 100 cycles.

The charge transfer resistances (R_{ct}) and Na^+ diffusion coefficients of NMTP/C@rGO and NMTP/C can be calculated from the fitted Nyquist plots (Fig. S12). The NMTP/C@rGO has an R_{ct} value of 172.8 Ω, much lower than that of NMTP/C (314 Ω). Based on the Na^+ diffusion coefficient equation and the fitted line in Fig. S12b, the Na^+ diffusion coefficients for NMTP/C and NMTP/C@rGO are 4.27×10^{-12} and 9.94×10^{-10} cm^2 s^{-1}, respectively. These values are significantly higher than those of other phosphate-based cathode materials (normally at the magnitude of $\sim 10^{-13}$ cm^2 s^{-1}).

The effect of annealing temperature on the sodium storage performance was also investigated. The NASICON structured NMTP can be obtained at an annealing temperature above 600 °C (Fig. S13). Among the samples prepared at 550, 600, and 650 °C, the sample prepared at 600 °C (NMTP/C@rGO) demonstrates the best Na storage performance (Fig. S14a). The sample prepared at 550 °C without a well crystallized NASICON structure displays no discharge plateaus and low capacity (Fig. S14). The sample prepared at 650 °C delivers a discharge capacity of 61 mAh g^{-1} with well developed discharge plateaus (Fig. S14b).

Ex-situ XPS was used to monitor the valence state of Mn of NMTP/C@rGO during charge/discharge. For the original NMTP/C@rGO, the Mn^{2+} dominates the sample although Mn^{3+} also exists (Fig. 4a) [48]. When charged to 4.2 V, the Mn^{4+} becomes the dominant Mn species, suggesting that Mn^{2+} and Mn^{3+} are oxidized during Na^+ extraction (Fig. 4b). When discharged to 2.5 V (Na^+ intercalation), most of the Mn^{3+} and Mn^{4+} are reduced to Mn^{2+} (Fig. 4c). For *in-situ* XRD (Fig. 4d, S15), the (113), (204), and (116) diffractions of NMTP shift to higher angles during charging and turn back to the original positions in the following discharge. This indicates the corresponding lattice spacing contract during charging and expands during discharging. Take the d_{113} as an example, the spacing contracts from 3.81 to 3.61 Å during

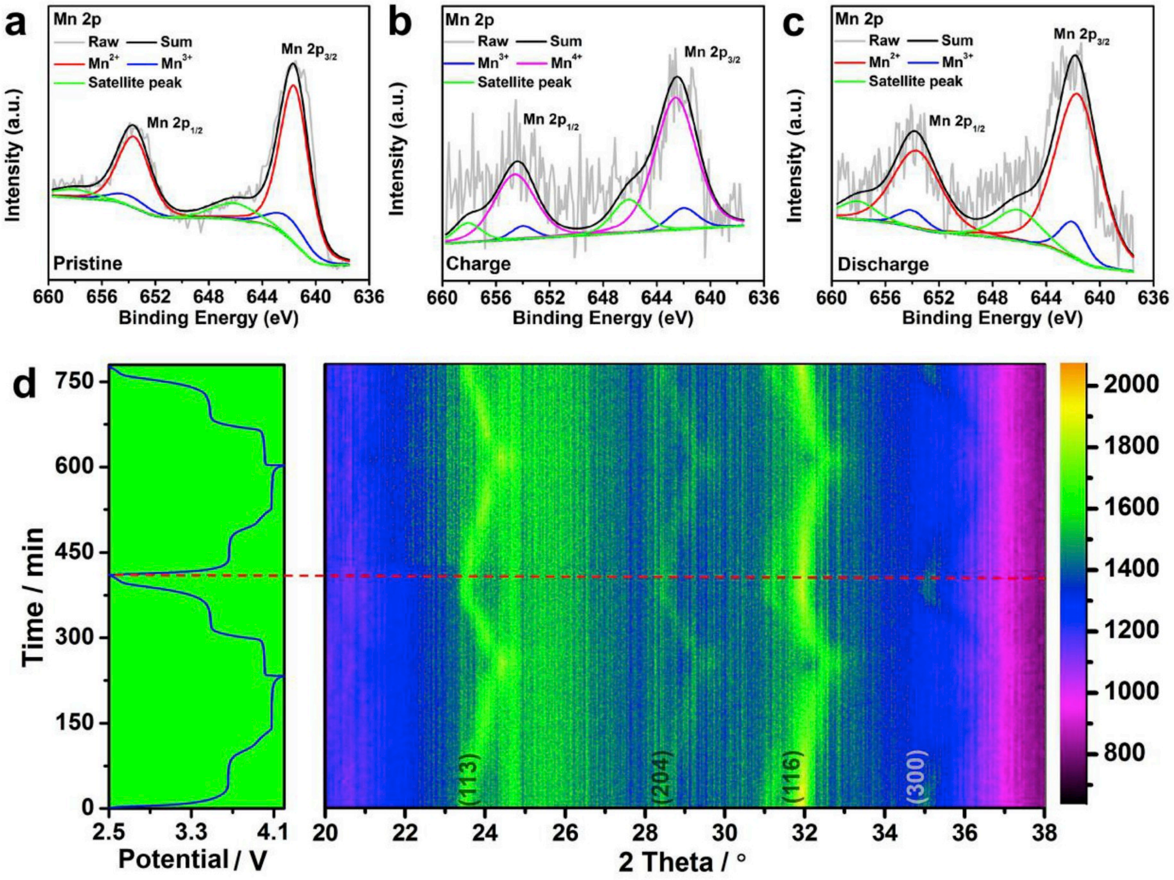

Fig. 4. *Ex-situ* XPS spectra of NMTP/C@rGO collected at different electrochemical states at 0.2 C: (a) initial state, (b) charged to 4.2 V, and (c) discharged to 2.5 V. (d) *In-situ* XRD patterns of NMTP/C@rGO during galvanostatic charge/discharge at a current density of 50 mA g^{-1}.

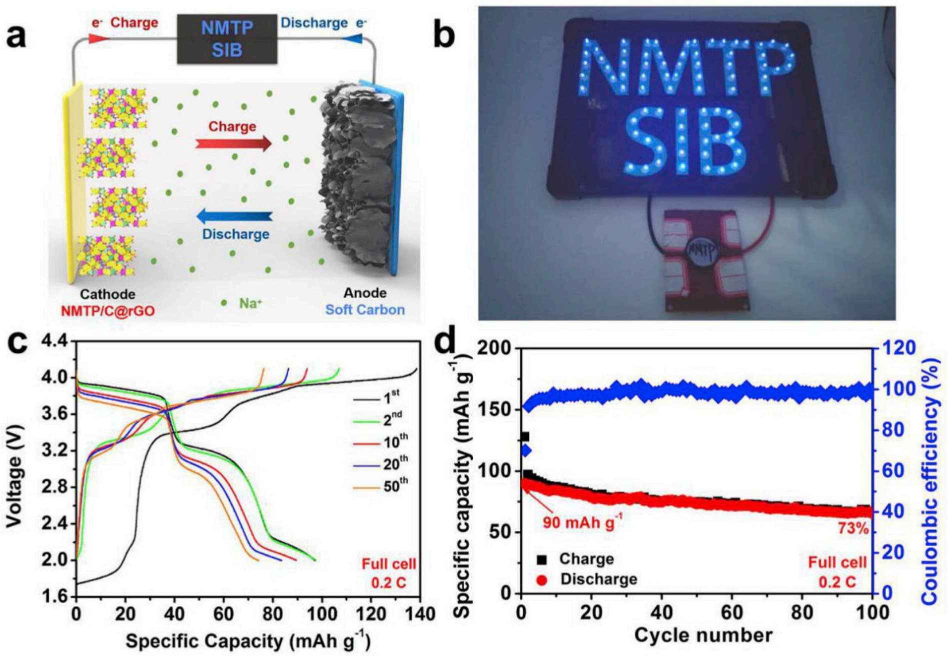

Fig. 5. (a) Schematic illustration of the NMTP/C@rGO//SC full cell; (b) lighted LED belts powered by an NMTP/C@rGO//SC full cell; (c) representative charge/discharge curves of the NMTP/C@rGO//SC full cell; (d) cycling performance of the NMTP/C@rGO//SC full cell at 0.2 C.

charging and expands to 3.81 Å during discharging (Fig. S16). The (300) peak disappears upon charging and re-appears upon discharging. At the end of first discharge process, each peak can be recovered to their original positions, demonstrating the excellent reversibility of de-sodiation/sodiation processes. The above results demonstrate that the de-sodiation/sodiation of NMTP/C@rGO involves both solid-solution and two-phase reactions.

Full cells were assembled using NMTP/C@rGO as the cathode material and soft carbon (SC) as the anode material. The schematic illustration of NMTP/C@rGO//SC full cell and its working mechanism during charge/discharge are shown in Fig. 5a. Before full cell assembly, the structure of soft carbon was characterized by SEM, XRD, and Raman spectra (Fig. S17), while the electrochemical performance was characterized by galvanastatic charge/discharge (Fig. S18). After full charging, the full cell is capable of lighting an LED screen (Fig. 5b). Based on the mass of NMTP/C@rGO, the NMTP/C@rGO//SC full cell delivers an initial discharge capacity of 97 mAh g^{-1} at 0.2 C. After 100 cycles, it retains a capacity retention ratio of 73%. The initial coulombic efficiency is 70.1%, and the coulombic efficiency increases to around 99% in the following cycles (Fig. 5c and d). The half-cell and full cell results demonstrate that the NMTP/C@rGO is a promising cathode material for SIBs.

4. Conclusion

In summary, a facile spray-drying assisted approach has been developed to fabricate reduced graphene oxide and semi-graphitic carbon co-decorated $Na_3MnTi(PO_4)_3$ microspheres. When employed as the SIB cathode, the dual carbon functionalized NMTP manifests a high discharge capacity of 114 mAh g^{-1}, corresponding to a high energy density of 410 Wh kg^{-1} at 0.2 C. Benefiting from the dual carbon decoration, high rate capability, and long-term durability have also been demonstrated. Sodium-ion full-cells have also been assembled using NMTP/C@rGO as the cathode and soft carbon as the anode. The impressive electrochemical performances make the NMTP/C@rGO microspheres a promising cathode material for SIBs.

Declaration of competing interest

The authors declare that they have no known competing financial interests or personal relationships that could have appeared to influence the work reported in this paper.

Acknowledgments

This work was supported by the National Natural Science Foundation of China (21673171, 51521001), and the China Scholarship Council under Grant No. 201806950020.

Appendix A. Supplementary data

Supplementary data to this article can be found online at https://doi.org/10.1016/j.nanoen.2020.104548.

References

[1] H. Li, H. Tang, C. Ma, Y. Bai, J. Alvarado, B. Radhakrishnan, S. Ong, F. Wua, Y. Meng, C. Wu, Chem. Mater. 30 (2018) 2498–2505.
[2] F. Wu, C. Zhao, S. Chen, Y. Lu, Y. Hou, Y. Hu, J. Maier, Y. Yu, Mater. Today 21 (2018) 960–973.
[3] S.P. Ong, V.L. Chevrier, G. Hautier, A. Jain, C. Moore, S. Kim, X. Ma, G. Ceder, Energy Environ. Sci. 4 (2011) 3680–3688.
[4] Q. Ni, Y. Bai, F. Wu, C. Wu, Adv. Sci. 4 (2017) 1600275.
[5] N. Yabuuchi, K. Kubota, M. Dahbi, S. Komaba, Chem. Rev. 114 (2014) 11636–11682.
[6] T. Jin, Q. Han, L. Jiao, Adv. Mater. 32 (2020) 1806304.
[7] J.Y. Hwang, S.T. Myung, Y.K. Sun, Chem. Soc. Rev. 46 (2017) 3529–3614.
[8] T. Jin, Y. Liu, Y. Li, K. Cao, X. Wang, L. Jiao, Adv. Energy Mater. 7 (2017) 1700087.
[9] D. Kundu, E. Talaie, V. Duffort, L.F. Nazar, Angew. Chem. Int. Ed. 54 (2015) 3431–3448.
[10] A. Ponrouch, R. Dedryvere, D. Monti, A.E. Demet, J.M.A. Mba, L. Croguennec, C. Masquelier, P. Johansson, M.R. Palacín, Energy Environ. Sci. 6 (2013) 2361–2369.
[11] L.P. Wang, L. Yu, X. Wang, M. Srinivasan, Z. Xu, J. Mater. Chem. A 3 (2015) 9353–9378.
[12] C. Fang, Y. Huang, W. Zhang, J. Han, Z. Deng, Y. Cao, H. Yang, Adv. Energy Mater. 6 (2016) 1501727.
[13] T. Liu, Y. Zhang, Z. Jiang, X. Zeng, J. Ji, Z. Li, X. Gao, M. Sun, Z. Lin, M. Ling, J. Zheng, C. Liang, Energy Environ. Sci. 12 (2019) 1512–1533.
[14] W. Ren, M. Qin, Z. Zhu, M. Yan, Q. Li, L. Zhang, D. Liu, L. Mai, Nano Lett. 17 (2017) 4713–4718.
[15] Y. Yue, A.J. Binder, B. Guo, Z. Zhang, Z.A. Qiao, C. Tian, S. Dai, Angew. Chem. Int. Ed. 53 (2014) 3134–3137.
[16] L. Wang, J. Song, R. Qiao, L.A. Wray, M.A. Hossain, Y.-D. Chuang, W. Yang, Y. Lu, D. Evans, J.-J. Lee, S. Vail, X. Zhao, M. Nishijima, S. Kakimoto, J.B. Goodenough, J. Am. Chem. Soc. 137 (2015) 2548–2554.
[17] X. Liu, Y. Tan, T. Liu, W. Wang, C. Li, J. Lu, Y. Sun, Adv. Funct. Mater. 29 (2019) 1903795.
[18] W. Pang, S. Kalluri, V.K. Peterson, N. Sharma, J. Kimpton, B. Johannessen, H. K. Liu, S.X. Dou, Z. Guo, Chem. Mater. 27 (2015) 3150–3158.
[19] Y. Zhou, P. Wang, Y. Niu, Q. Li, X. Yu, Y. Yin, S. Xu, Y. Guo, Nano Energy 55 (2019) 143–150.
[20] Y. Xie, H. Wang, G. Xu, J. Wang, H. Sheng, Z. Chen, Y. Ren, C.J. Sun, J. Wen, J. Wang, D.J. Miller, J. Lu, K. Amine, Z.F. Ma, Adv. Energy Mater. 6 (2016) 1601306.
[21] H.-H. Sun, J.-Y. Hwang, C.S. Yoon, A. Heller, C.B. Mullins, ACS Nano 12 (2018) 12912–12922.
[22] C. An, Y. Yuan, B. Zhang, L. Tang, B. Xiao, Z. He, J. Zheng, J. Lu, Adv. Energy Mater. 9 (2019) 1900356.
[23] D. Chao, C.M. Lai, P. Liang, Q. Wei, Y. Wang, C.R. Zhu, G. Deng, V.V.T. Doan-Nguyen, J. Lin, L. Mai, H. Fan, B. Dunn, Z. Shen, Adv. Energy Mater. 8 (2018) 1800058.
[24] R. Rajagopalan, B. Chen, Z. Zhang, X. Wu, Y. Du, Y. Huang, B. Li, Y. Zong, J. Wang, G.H. Nam, M. Sindoro, S.X. Dou, H.K. Liu, H. Zhang, Adv. Mater. 29 (2017) 1605694.
[25] X. Wang, C. Niu, J. Meng, P. Hu, X. Xu, X. Wei, L. Zhou, K. Zhao, W. Luo, M. Yan, L. Mai, Adv. Energy Mater. 5 (2015) 1500716.
[26] Y.-U. Park, D.-H. Seo, H.-S. Kwon, B. Kim, J. Kim, H. Kim, I. Kim, H.-I. Yoo, K. Kang, J. Am. Chem. Soc. 135 (2013) 13870–13878.
[27] P. Senguttuvan, G. Rousse, M.E.A.Y.D. Dompablo, H. Vezin, J.M. Tarascon, M. R. Palacín, J. Am. Chem. Soc. 135 (2013) 3897–3903.
[28] Y. Jiang, Z. Yang, W. Li, L. Zeng, F. Pan, M. Wang, X. Wei, G. Hu, L. Gu, Y. Yu, Adv. Energy Mater. 5 (2015) 1402104.
[29] X. Jiang, Z. Zeng, L. Xiao, X. Ai, H. Yang, Y. Cao, ACS Appl. Mater. Interfaces 9 (2017) 43733–43738.
[30] Y. Fang, L. Xiao, J. Qian, Y. Cao, X. Ai, Y. Huang, H. Yang, Adv. Energy Mater. 6 (2016) 1502197.
[31] Y. Jiang, X. Zhou, D. Li, X. Cheng, F. Liu, Y. Yu, Adv. Energy Mater. 8 (2018) 1800068.
[32] F. Chen, V.M. Kovrugin, R. David, O. Mentré, F. Fauth, J.N. Chotard, C. Masquelier, Small Methods 4 (2018) 1800218.
[33] M.J. Aragón, P. Lavela, G.F. Ortiz, J.L. Tirado, ChemElectroChem 2 (2015) 995–1002.
[34] R. Liu, G. Xu, Q. Li, S. Zheng, G. Zheng, Z. Gong, Y. Li, E. Kruskop, R. Fu, Z. Chen, K. Amine, Y. Yang, ACS Appl. Mater. Interfaces 9 (2017) 43632–43639.
[35] W. Zhou, L. Xue, X. Lü, H. Gao, Y. Li, S. Xin, G. Fu, Z. Cui, Y. Zhu, J.B. Goodenough, Nano Lett. 16 (2016) 7836–7841.
[36] H. Li, T. Jin, X. Chen, Y. Lai, Z. Zhang, W. Bao, L. Jiao, Adv. Energy Mater. 8 (2018) 1801418.
[37] H. Wang, T. Zhang, C. Chen, M. Ling, Z. Lin, S. Zhang, F. Pan, C. Liang, Nano Res. 11 (2018) 490–498.
[38] F. Zhang, W. Li, X. Xiang, M. Sun, Chem. Eur J. 23 (2017) 12944–12948.
[39] H. Li, Y. Bai, F. Wu, Q. Ni, C. Wu, ACS Appl. Mater. Interfaces 8 (2016) 27779–27787.
[40] H. Gao, Y. Li, K. Park, J.B. Goodenough, Chem. Mater. 28 (2016) 6553–6559.
[41] T. Zhu, P. Hu, X. Wang, Z. Liu, W. Luo, K.A. Owusu, W. Cao, C. Shi, J. Li, L. Zhou, L. Mai, Adv. Energy Mater. 9 (2019) 1803436.
[42] H. Gao, J.B. Goodenough, Angew. Chem. Int. Ed. 55 (2016) 12768–12772.
[43] C. Zhu, C. Wu, C.-C. Chen, P. Kopold, P.A. van Aken, J. Maier, Y. Yu, Chem. Mater. 29 (2017) 5207–5215.
[44] H. Wang, C. Chen, C. Qian, C. Liang, Z. Lin, RSC Adv. 7 (2017) 33273–33277.
[45] U. Nisar, R.A. Shakoor, R. Essehli, R. Amin, B. Orayech, Z. Ahmad, P.R. Kumar, R. Kahraman, S. Al-Qaradawi, A. Soliman, Electrochim. Acta 292 (2018) 98–106.
[46] H. Gao, I.D. Seymour, S. Xin, L. Xue, G. Henkelman, J.B. Goodenough, J. Am. Chem. Soc. 140 (2018) 18192–18199.
[47] P.R. Kumar, A. Kheireddine, U. Nisar, R.A. Shakoor, R. Essehli, R. Amin, I. Belharouak, J. Power Sources 429 (2019) 149–155.
[48] L. Chen, B. Yan, Y. Xie, S. Wang, X. Jiang, G. Yang, J. Power Sources 261 (2014) 188–197.

Ting Zhu received her Master degree from Tianjin Polytechnic University in 2016. She is currently working toward the Ph.D. degree at Wuhan University of Technology and her current research focuses on sodium-ion batteries.

Ping Hu received his Master degree from Wuhan University of Technology in 2016. He is currently working toward the Ph.D. degree at Wuhan University of Technology and his current research focuses on energy storage materials.

Congcong Cai received his B.S. degree in Wuhan University of Science and Technology in 2017. He is currently working toward the Ph.D. degree at Wuhan University of Technology and his current research focuses on sodium-ion batteries.

Ziang Liu received his B.S. degree in Wuhan University of Technology in 2017. He is currently working toward the Ph.D. degree at Wuhan University of Technology and his current research involves energy materials and devices.

Guangwu Hu received his B.S. degree in Taiyuan Institute of Technology in 2013. He received the Master degree at Wuhan University of Technology in 2017. He is currently a Ph.D. candidate at Wuhan University of Technology and his research focuses on lithium-ion batteries.

Quan Kuang received his Ph.D. degree from School of Materials Science and Engineering, South China University of Technology in 2012. After graduation, he worked as a senior engineer on cathode development at Amperex Technology Limited (2012–2013). He is now an associate professor at the South China University of Technology. His research interests mainly focus on novel materials for advanced secondary batteries.

Liqiang Mai is a Chair Professor at the School of Materials Science and Engineering, Wuhan University of Technology. He is the winner of the National Natural Science Fund for Distinguished Young Scholars and Fellow of the Royal Society of Chemistry. He received his Ph.D. from Wuhan University of Technology in 2004 and carried out his postdoctoral research with Prof. Zhong Lin Wang at Georgia Institute of Technology in 2006–2007. He worked as an advanced research scholar with Prof. Charles M. Lieber at Harvard University in 2008–2011 and Prof. Peidong Yang at University of California, Berkeley in 2017. His current research interests focus on new nanomaterials for electrochemical energy storage and micro/nano energy devices.

Liang Zhou received his Ph.D. degree from Department of Chemistry, Fudan University in 2011. After graduation, he worked as a postdoctoral research fellow at Nanyang Technological University (2011–2012) and The University of Queensland (2012–2015). He is now a full professor at Wuhan University of Technology. His research interests include functional nanomaterials for electrochemical energy storage.